Modeling Cyclic Deformation of HSLA Steels Using Crystal Plasticity

C. L. Xie

S. Ghosh*

M. Groeber

Computational Mechanics Research Laboratory,
Department of Mechanical Engineering,
The Ohio State University,
Columbus, OH 43210

High strength low alloy (HSLA) steels, used in a wide variety of applications as structural components are subjected to cyclic loading during their service lives. Understanding the cyclic deformation behavior of HSLA steels is of importance, since it affects the fatigue life of components. This paper combines experiments with finite element based simulations to develop a crystal plasticity model for prediction of the cyclic deformation behavior of HSLA-50 steels. The experiments involve orientation imaging microscopy (OIM) for microstructural characterization and mechanical testing under uniaxial and stress–strain controlled cyclic loading. The computational models incorporate crystallographic orientation distributions from the OIM data. The crystal plasticity model for bcc materials uses a thermally activated energy theory for plastic flow, self and latent hardening, kinematic hardening, as well as yield point phenomena. Material parameters are calibrated from experiments using a genetic algorithm based minimization process. The computational model is validated with experiments on stress and strain controlled cyclic loading. The effect of grain orientation distributions and overall loading conditions on the evolution of microstructural stresses and strains are investigated. [DOI: 10.1115/1.1789966]

Keywords: Crystalline Plasticity, Constitutive Equation, Misorientation, Parameter Calibration, Cyclic Deformation

1 Introduction

High strength low alloy (HSLA) steels are a group of low carbon steels designed to provide special combination of properties such as strength, toughness, formability, weldability, and corrosion resistance [1]. These steels contain small amounts of alloying elements to attain high initial yield strength by strengthening the ferrite, promoting precipitation hardenability, and by helping to control grain size. HSLA steels are used in a wide variety of applications such as structural components of vehicles, pressure vessels, line pipes, etc. Understanding the cyclic deformation behavior of HSLA steels is of technological importance, since many of the structural applications are subjected to cyclic loading during their service lives. The fatigue life is strongly linked to the cyclic stress or strain state in a critical region. A number of investigations on the mechanical response and fracture behavior of HSLA steels have been carried out in the past thirty years and have been discussed by Suresh in [2]. Various experimental studies on this issue have been reported in [3–6]. Observations of fatigue life have been linked to physical phenomena like elevated cyclic stress amplitudes, which can lead to microyielding and causing persistent slip bands. These are known microcrack initiation sites in many alloys. Significant efforts have been also made in the modeling of the fatigue behavior of HSLA steels. Chung et al. have studied the low-cycle fatigue behavior in HSLA steel at plastic strain amplitudes ranging from 1×10^{-5} to 1×10^{-2} in [7]. They found that microcracks are initiated along slip lines in both air and vacuum. Many phenomenological models have been proposed to model cyclic deformation and fatigue [1–9]. These models however lack the explanation of physically observed phenomena, such as single slip at low plastic strain amplitudes or the hysteresis memory [10]. In metallic materials, significant variations in stress histories may be experienced by crystals in the polycrystalline aggregate, even when they are subjected to a macroscopically uniform cyclic loading history [11]. Some of the newly developed crystal plasticity models [10–16] are able to include many physical elements and can help in the understanding of cyclic plasticity phenomena. During cyclic loading, the state of microscale stress in a metallic material with a polycrystalline microstructure depends on the orientation of the grain with respect to the loading directions as well as with respect to the orientations of its neighbors, the material crystal properties and other factors. Studies with numerical calculations [11] have shown that depending on the loading conditions, significant stress gradients and plastic strain can arise within the polycrystalline aggregate associated with a continuum point, and even within a single grain.

This paper invokes a combination of experiments and finite element based simulations to develop a physically based crystal plasticity model for prediction of the cyclic deformation behavior of HSLA-50 steels. It involves microstructural characterization and incorporation of crystallographic orientation distribution to models, based on accurate microstructural data obtained by orientation imaging microscopy. Mechanical testing is performed under uniaxial testing as well as for stress and strain controlled cyclic loading. Material response, including cyclic hardening or softening, mean stress relaxation, cyclic creep deformation and rate dependence, depends on the control modes. The crystal plasticity model for bcc materials uses a thermally activated energy theory for plastic flow, self and latent hardening, kinematic hardening, as well as yield point phenomena. A genetic algorithm based minimization process is used to calibrate crystal plasticity parameters from experimental data. The computational model is validated with experiments on stress and strain controlled cyclic loading. Finally, the effect of grain orientation distributions and overall loading conditions on the evolution of microstructural stresses and strains are investigated.

2 Material Characterization and Mechanical Testing

The constitutive models are developed from mechanical tests conducted with samples of galvanneal, high strength low alloy

*Corresponding author. Tel.: +1-614-292-2599; Fax: 614-292-3163; e-mail address: ghosh.5@osu.edu

Contributed by the Materials Division for publication in the JOURNAL OF ENGINEERING MATERIALS AND TECHNOLOGY. Manuscript received by the Materials Division October 21, 2003; revision received April 6, 2004. Associate Editor: M. P. Miller.

Table 1 Nominal chemical composition (wt. %) of HSLA-50 steel

C	Mn	N	P	S	Si	Al	Ti	Ni
0.054	0.400	0.005	0.064	0.014	0.014	0.040	0.002	0.040

steel or HSLA-50 grade with 50 ksi minimum yield strength. Specimens are extracted from 1.57 mm thick plates of cold-rolled and strain aged HSLA, provided by ISPAT-Inland Steel. The nominal composition of this steel is given in Table 1 and a SEM micrograph of the microstructure is shown in Fig. 1(a). The major phase in this material, as observed from the micrograph, is equiaxed grains of ferrite with bcc crystallographic structure. While small traces (less than 5% by volume) of various sulfides and carbides are present along the ferrite grain boundaries, the pearlite concentration is insignificant. The grain size distribution depicted in Fig. 1(b) indicates a range from 3 μm to 30 μm, with an average size of 10 μm.

2.1 Crystallographic Orientations. The crystallographic texture, representing the orientation distribution of all crystallites, is measured by orientation imaging microscopy (OIM), involving electron back-scattered diffraction (EBSD) in scanning electron microscopy. According to Bunge's convention [17] of orientation measurement, the grain orientation g is identified by the Euler angle set $(\varphi_1, \Phi, \varphi_2)$. The orientation distribution function (ODF) is a function of the Euler angle set [17] $f(g) = (\Delta N/N)/\Delta g$, where N is the total number of crystallites in the domain analyzed, ΔN is the number of additional crystallites which possess orientation between the sets g and $g + \Delta g$. Figure 2(a) is a three-dimensional surface plot of the ODF's $f(g)$ drawn within a bounding box of the 3D Euler angle space. The isosurfaces represent a range from 50% ($f(g) = 1.92$) to 100% ($f(g) = 3.83$) of the maximum value of the ODF data. Isosurfaces of higher values are enveloped within those of lower values of ODF. This can be observed from the intersection with the plane $\varphi_1 = 0$, where the highest value region is near the middle. Figure 2(b) shows skeleton lines of typical textures and points of ideal orientations for bcc steels. It can be seen that the most important orientation fibers of HSLA-50 steel are the α-fiber with $\langle 110 \rangle$ parallel to rolling direction (RD) and the γ-fiber with $\langle 111 \rangle$ parallel to normal direction (ND). If local orientations are divided into 20° intervals, four orientation components with large volume fractions are found. They are $\{112\}\langle 110 \rangle$, $\{001\}\langle 110 \rangle$, $\{111\}\langle 112 \rangle$, and $\{111\}\langle 110 \rangle$. The first two components belong to the α-fiber while the last two components belong to the γ-fiber.

2.2 Mechanical Properties. Engineering design for many load-bearing components, especially with cyclic loading for fatigue analysis, assumes peak macroscopic stresses in the elastic

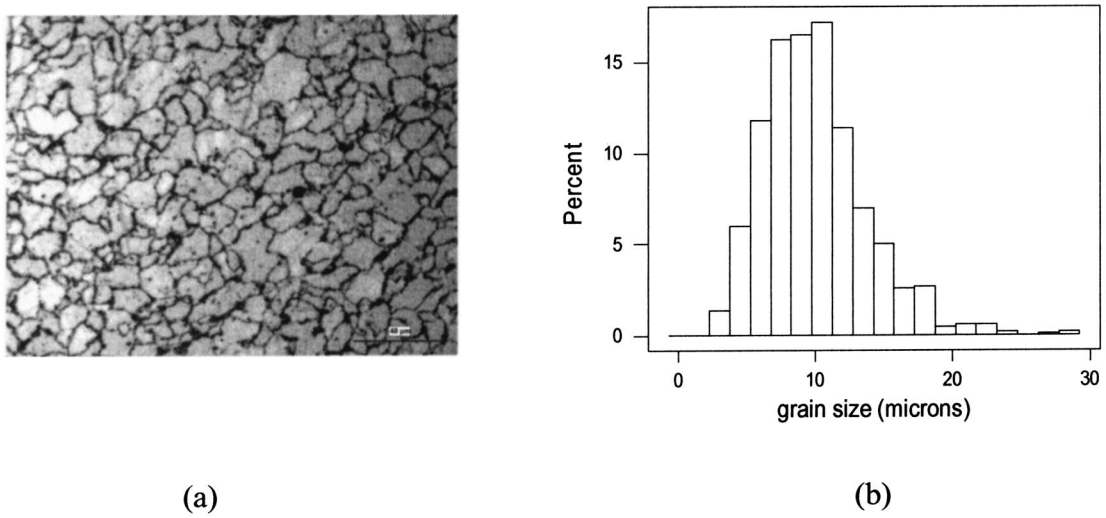

Fig. 1 (*a*) Scanning electron micrograph of the microstructure of HSLA-50 steel; (*b*) Distribution of grain size

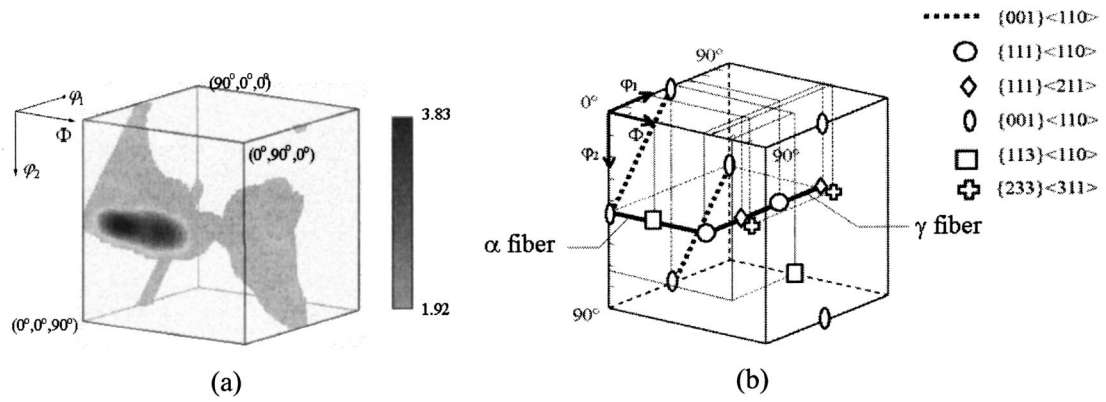

Fig. 2 (*a*) Contour plot of the ODF in 3D Euler angle space, ranging from 50% to the maximum value of ODF; (*b*) Reduced Euler space with typical fibers and orientations of HSLA-50 steel

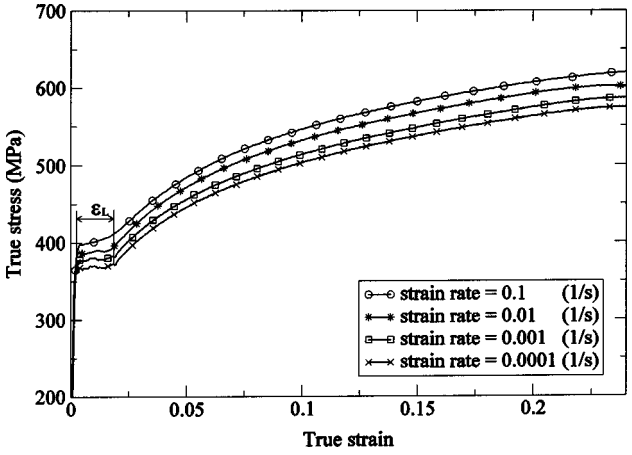

Fig. 3 Stress–strain data for uniaxial loading at four strain rates

range. However, when the microstructure is considered, the crystal structure, orientation and material anisotropy can cause the local stresses to exceed the elastic limit. Therefore, a proper constitutive model that can describe the yield-point phenomena as well as the subsequent cyclic plasticity behavior is essential for accurate analysis. The mechanical properties of the strain aged HSLA-50 steel are tested in the as-received state. All specimens are cut in the rolling direction (RD). Three types of room temperature experiments are performed for mechanical property evaluation, namely (i) uniaxial tension at different strain rates, (ii) strain-controlled cyclic tests, and (iii) stress-controlled cyclic loading tests.

2.2.1 Uniaxial Tension. Uniaxial tests are conducted following ASTM E8 standard methods of tension testing for metallic materials [18]. The stress–strain plots at four different strain rates, viz., $\dot{\varepsilon}=0.1\ s^{-1}$, $0.01\ s^{-1}$, $0.001\ s^{-1}$, and $0.0001\ s^{-1}$, are depicted in Fig. 3. HSLA steels, like many bcc metals, exhibit a significant yield point phenomena in the stress–strain behavior. The yield plateau (called Lüders strain) is observed in these plots, resulting from the formation and propagation of Lüders-bands as explained in [18–20]. The experiments show a sharp yield point followed by an abrupt drop in the yield stress to a plateau for fully annealed HSLA steels that are not tempered or tension-leveled. The Lüders strain ε_L (see Fig. 3) has been reported to increase with increasing strain rates for mild steels in [19]. However, the experiments in the present study did not reveal significant rate dependence of the Lüders strain within the range from $0.1\ s^{-1}$ to $0.0001\ s^{-1}$. The hardening description of the stress–strain curve of HSLA-50 steel can be divided into three phases, viz. (a) a region of rapid hardening with saturation from the initial yield point to the end of the yield plateau; (b) a region of increasing slope after the yield plateau; and (c) a region of decreasing slope caused by saturation of plastic hardening.

2.2.2 Strain and Stress Controlled Cyclic Tests. Strain controlled cyclic tests are more common for low cycle fatigue analysis, especially in the ground vehicle industry. On the other hand, the stress-controlled mode is mostly used in structures for high cycle fatigue design. A significant difficulty arises in cyclic tension-compression testing of sheet materials due to buckling in the compression phase. Various efforts have been made to avoid this problem, e.g., involving small gage length and incorporating Woods metal grip for better alignment with reduced eccentricity [20]. Yoshida [19,21] has increased the specimen thickness by bonding two or more plates with adhesives, and has used a special specimen holder for in-plane cyclic tests of sheet metals. In the present study, a special device designed by Wagoner et al. [22], as

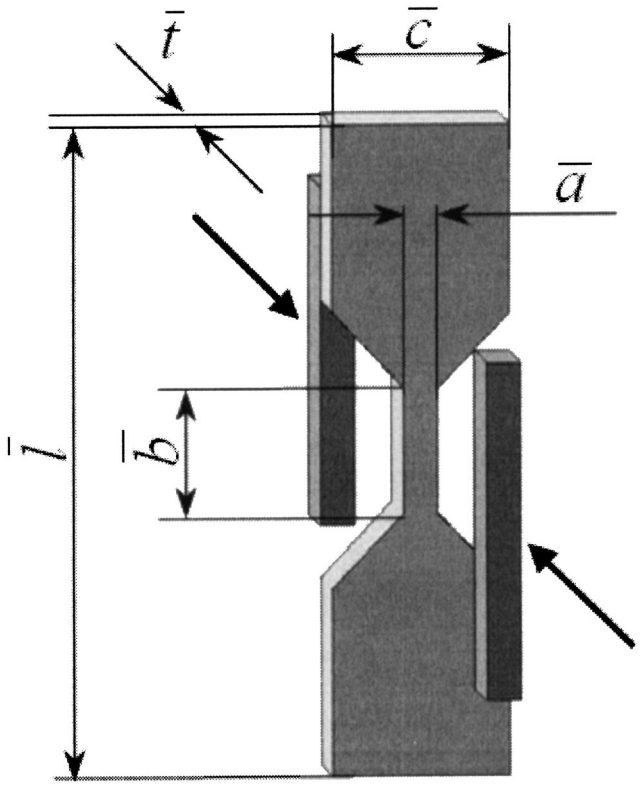

Fig. 4 Schematic diagram of the specimen assembly for cyclic tension-compression tests

shown in Fig. 4, is used. The dimensions of the specimen and device are: $\bar{a}=0.6$ in., $\bar{b}=1.45$ in., $\bar{c}=2.0$ in., $\bar{l}=8.0$ in., $\bar{t}=0.062$ in. In this device, two hydraulic pressure driven holders provide the clamping force on the surfaces of the specimen to prevent it from bucking. Teflon sheets are inserted at the interface between the holder and specimen to reduce the friction. The combined action of applied tension-compression, lateral pressure and interfacial friction force, produces a predominantly biaxial state of stress (σ_{11}, σ_{22}) in the material, even though the pressure is small. Equivalent stress–strain plots are therefore generated from the stress states to simulate the uniaxial tension/compression response. Details of this process in provided in [23]. The first set of tests conducted is strain-controlled cyclic loading, having triangular waveforms with peak strains of 0.0045 and 0.015, respectively, at a constant strain rate of $5.8\times10^{-4}\ s^{-1}$. The corresponding stress–strain responses for five cycles are illustrated in Figs. 5(a) and (b). Cyclic hardening, manifested by an increase in the stress amplitude with cyclic straining, is evident in the first few cycles for the case with a peak strain of 0.015, as shown in Fig. 5(b). No cyclic hardening is observed for the case with a smaller peak strain. This observation is consistent with strain-range dependent cyclic hardening behavior, which has been discussed and modeled with anisotropic hardening in [19,24]. The Bauschinger effect can be attributed to the short-range interactions between dislocations, interstitials, precipitates and other barriers, as well as the long-range interaction among individual grains. This is also observed even in the small cyclic strain ranges. Finally, a stress-controlled cyclic test is conducted with a servo-hydraulic test machine. The load is characterized by a triangular waveform with an applied stress rate of $\dot{\sigma}=46.5$ (MPa/s), peak stress amplitude $\sigma_{max}=380.0$ (MPa), and R-ratio is $\sigma_{min}/\sigma_{max}=-0.7$. In the case of fully-reversed strain-controlled tests, the stresses increase initially with each cycle until a stable state is achieved. The occurrence of plastic deformation causes mean stress relaxation, which takes

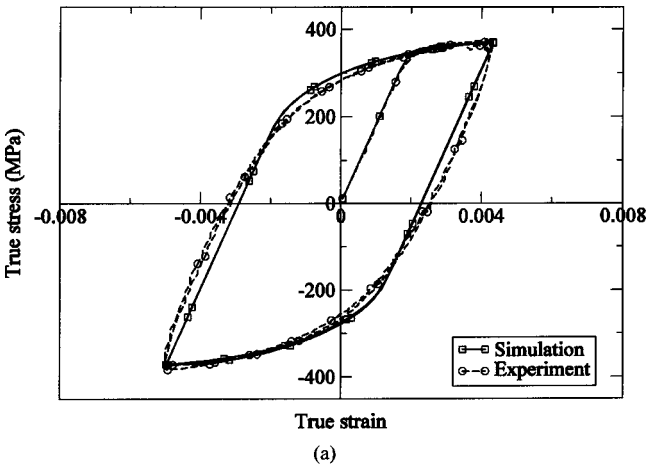

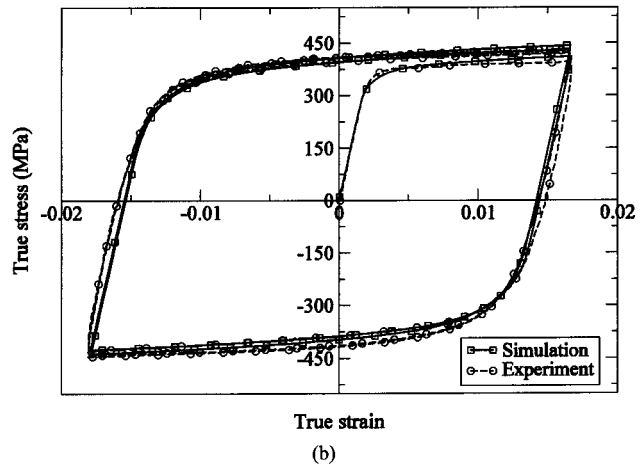

Fig. 5 Experimental and simulated stress–strain responses in the strain-controlled cyclic tests with peak strain amplitudes of (*a*) 0.0045; (*b*) 0.015

place in the early stage of life. Therefore the fatigue life is not appreciably affected by the introduction of a mean strain. For fully-reversed stress-controlled tests with rate dependent materials, the cyclic plastic strain or ratcheting strain increases with the number of cycles until a stable response called shakedown is achieved. In addition to microstructural characteristics, fatigue life for stress-controlled tests depend on many factors like mean stress, stress amplitude, frequency, and loading history.

3 Material Description and Model

3.1 Constitutive Relations. The material studied is a HSLA steel which has a body centered cubic or bcc crystal structure. The bcc crystals consist of 48 possible slip systems including $\{110\}\langle 111\rangle$, $\{112\}\langle 111\rangle$ and $\{123\}\langle 111\rangle$ along which crystallographic slip can occur. The different slip systems cause HSLA steels to exhibit strong anisotropic behavior both in elasticity and in plasticity. For elasticity, a cubic response with three independent elastic constants (C_{11}, C_{12}, C_{44}) is assumed for modeling the anisotropy. Plastic deformation occurs by crystallographic slip on the different slip systems. The deformation behavior of HSLA steel is modeled using a rate and temperature-dependent, elastic-plastic, finite strain, crystal plasticity formulation following the work of Anand et al. [25,26]. In this model, crystal deformation results from a combination of the elastic stretching and rotation of the crystal lattice and plastic slip on the different slip systems. The stress–strain relation is written in terms of the second Piola–Kirchoff stress ($\mathbf{S}=\det\mathbf{F}^e\mathbf{F}^{e^{-1}}\boldsymbol{\sigma}\mathbf{F}^{e^{-T}}$) and the work conjugate Lagrange Green strain tensor ($\mathbf{E}^e\equiv(1/2)\{\mathbf{F}^{eT}\mathbf{F}^e-\mathbf{I}\}$) as

$$\mathbf{S}=\boldsymbol{C}:\mathbf{E}^e \tag{1}$$

where $\boldsymbol{C}$ is a fourth order anisotropic elasticity tensor, $\boldsymbol{\sigma}$ is the Cauchy stress tensor, and $\mathbf{F}^e$ is an elastic deformation gradient defined by the relation

$$\mathbf{F}^e\equiv\mathbf{F}\mathbf{F}^{p^{-1}},\quad \det\mathbf{F}^e>0, \tag{2}$$

$\mathbf{F}$ and $\mathbf{F}^p$ are the deformation gradient and its plastic component respectively with the incompressibility constraint $\det\mathbf{F}^p=1$. The flow rule governing evolution of plastic deformation is expressed in terms of the plastic velocity gradient as

$$\mathbf{L}^p=\dot{\mathbf{F}}^p\mathbf{F}^{p^{-1}}=\sum_\alpha\ \dot\gamma^\alpha\mathbf{s}_0^\alpha. \tag{3}$$

where the Schmidt tensor is expressed as $\mathbf{s}_0^\alpha\equiv\mathbf{m}_0^\alpha\otimes\mathbf{n}_0^\alpha$ in terms of the slip direction ($\mathbf{m}_0^\alpha$) and slip plane normal ($\mathbf{n}_0^\alpha$) in the reference configuration, associated with αth slip system. For the plastic shearing rate $\dot\gamma^\alpha$ on the slip system α, a number of crystalline plasticity models are based on a power law description [27,28]. This power law model is restricted to the high temperature range [29], and does not explicitly account for the rate and temperature sensitivity of plastic flow in crystalline materials under dynamic loading conditions and/or low homologous temperatures. Alternatively, a thermally activated theory of plastic law, postulated by Frost and Ashby [29], Kocks et al. [30], has been proven to accurately model a large range of strain rates and temperatures for bcc tantalum by Kothari and Anand [26]. In this law, the plastic shearing rate on a slip system α is written as

$$\dot\gamma^\alpha=\begin{cases}0 & \text{if}\quad \tau^\alpha_{\text{eff}}\leqslant 0\\ \dot\gamma^\alpha_*\exp\left\{-\dfrac{\Delta F}{k_BT}\left[1-\left(\dfrac{|\tau^\alpha_{\text{eff}}|}{s^\alpha_*}\right)^P\right]^Q\right\}\text{sign}(\tau^\alpha-\tau^\alpha_{\text{kin}}) & \text{if}\quad 0<\tau^\alpha_{\text{eff}}\leqslant s^\alpha_*\end{cases} \tag{4}$$

where $\dot\gamma^\alpha_*$ is a reference strain rate. The effective shear stress $\tau^\alpha_{\text{eff}}\ (=|\tau^\alpha|-s^\alpha_a)$ is the driving force for the dislocation motion on the slip system α, and is measured in terms of the resolved shear stress τ^α. The temperature dependent critical slip resistance s^α (>0), is assumed to be comprised of a part due to thermally activatable obstacles to slip s^α_* and a part due to the athermal obstacles to slip s^α_a, i.e., $s^\alpha=s^\alpha_*+s^\alpha_a$. The resistance to thermal obstacles for bcc metals is governed by interactions with Peierls resistance that increases with reduction in temperature. In Eq. (4), ΔF is the activation free energy, which is required to overcome the obstacles to slip without the aid of an applied shear stress, k_B is the Boltzmann's constant, $k_B=1.3807\times10^{-23}\ (\text{J}\cdot\text{K}^{-1})$, T is

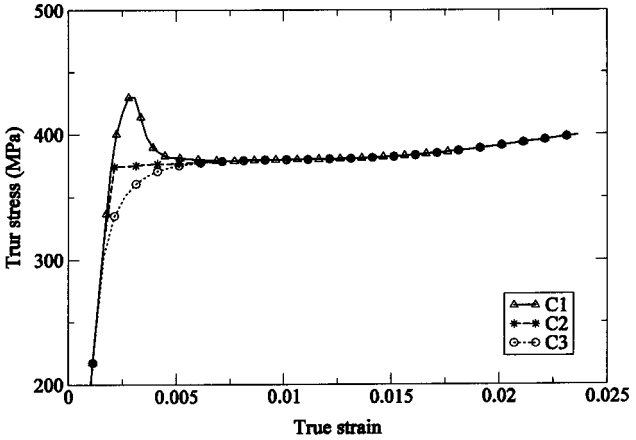

Fig. 6 Predicted yield point phenomena with variable reference strain rates

the absolute temperature; and $\boldsymbol{P}$ and $\boldsymbol{Q}$ are constant exponents. All the simulations in this work are carried out at room temperature, ~300 K.

In [26], the reference strain rate $\dot{\gamma}_*^\alpha$ has been taken to be a constant for all slip systems, with values in the range $\dot{\gamma}_0 \approx 10^6 - 10^7 ts^{-1}$. In reality, the mobile dislocation density, which contributes to $\dot{\gamma}_*^\alpha$ is a function of the applied stress, plastic deformation and temperature [30]. Consequently, the yield point phenomena as seen in the experimental plots of Fig. 3, which is due to rapid dislocation multiplication, cannot be captured with a constant $\dot{\gamma}_*^\alpha$. Following [19], $\dot{\gamma}_*^\alpha$ is expressed as a function of plastic strain as

$$\dot{\gamma}_*^\alpha = \dot{\gamma}_0 \left\{ \frac{\tanh[K^*(\bar{\varepsilon}^p - l_p)] + \tanh(Kl_p)}{\tanh(K) + \tanh(Kl_p)} \right\} + \dot{\gamma}_{\text{ini}} \tag{5}$$

where $\bar{\varepsilon}^p$ is the equivalent plastic strain defined as $\bar{\varepsilon}^p = \sqrt{\frac{2}{3}\varepsilon_{ij}^p \varepsilon_{ij}^p}$, and the Lagrangian plastic strain is defined as $\varepsilon_{ij}^p = \frac{1}{2}(F_{ij}^{pT} F_{ij}^p - \delta_{ij})$. Equation (5) assumes that $\dot{\gamma}_*^\alpha$ is the same for all slip systems initially and has a value $\dot{\gamma}_{\text{ini}} \approx 10 - 10^2\ \text{s}^{-1}$. It increases rapidly with plastic strain and approaches $\dot{\gamma}_0^\alpha$ in the asymptotic limit. K and l_p are material constants in this equation. The ability of the model to predict yield point phenomena under uniaxial tension is illustrated in Fig. 6, for three cases: (**C1**) $K = 1.25 \times 10^4$, $l_p = 1.2 \times 10^{-3}$, $\dot{\gamma}_{\text{ini}} = 1.0 \times 10^2$; (**C2**) $K = 1.0 \times 10^3$, $l_p = 2.2 \times 10^{-3}$, $\dot{\gamma}_{\text{ini}} = 1.0 \times 10^2$; and (**C3**) $\dot{\gamma}_* = \dot{\gamma}_0$. The stress–strain plot for (**C1**) shows a sharp yield point followed by the abrupt drop and the subsequent yield plateau, representing a fully annealed steel without any tempering. The curve for (**C2**) shows the yield plateau for the strain aged steel, whereas the plot for (**C3**) shows an unchanged value of $\dot{\gamma}_*^\alpha$. Evolution of the critical resolved slip resistance is assumed for the post-Lüders band propagation stage as

$$\dot{s}^\alpha = \begin{cases} 0 & \bar{\varepsilon}^p < \varepsilon_L^p \\ \dot{s}^\alpha & \bar{\varepsilon}^p \geq \varepsilon_L^p \end{cases} \tag{6}$$

where ε_L^p is the Lüder's strain. It should be noted that for cyclic loading, the yield point phenomena can occur only once for $\bar{\varepsilon}^p \geq \varepsilon_L^p$ at initial yielding. The hardening law of equation will be activated in the following cycles.

For pure bcc crystals, the athermal part of the slip resistance s_*^α is assumed to be constant, since it is controlled by the interactions with the Peierls lattice resistance [25]. Hence, following the description in [25,26]

$$\dot{s}^\alpha \approx \dot{s}_a^\alpha = \sum_\beta h^{\alpha\beta} |\dot{\boldsymbol{\gamma}}^\beta|; \quad h^{\alpha\beta} = [q + (1-q)\boldsymbol{\delta}^{\alpha\beta}] h^\beta;$$

$$h^\beta = h_0^\beta \left| 1 - \frac{s^\beta}{s_s^\beta} \right|^r \text{sign}\left(1 - \frac{s^\beta}{s_s^\beta} \right) \tag{7}$$

where $h^{\alpha\beta}$ is a deformation dependent rate of change of the deformation resistance on slip system α due to shearing on slip system β and describes both self and latent hardening of the slip systems. The parameter h^β denotes the self-hardening rate describing both hardening and softening, q is a latent-hardening parameter chosen to be 1.4, h_0^β is the initial hardening rate, s_s^β is the saturation value of reference shear stress, and r is a constant exponent. The use of absolute value of $|\dot{\boldsymbol{\gamma}}^\beta|$ in the hardening equation is due to the fact that hardening is not affected by the direction of shearing on slip systems. The variables s_*^α and s_s^β are taken to be the same for all slip systems.

Kinematic hardening plays an important role in cyclic plasticity, strain localization and plastic strain ratcheting under cycling loading. In an attempt to include this feature in the flow rule of Eq. (4), the effective resolved stress τ_{eff}^α on the slip system $\alpha$is modified as:

$$\tau_{\text{eff}}^\alpha = |\tau^\alpha - \tau_{\text{kin}}^\alpha| - s_a^\alpha \tag{8}$$

where τ_{kin}^α is the resolved backstress or the projection of the back stress tensor σ_{kin} on the slip system α, expressed as

$$\tau_{\text{kin}}^\alpha = (\boldsymbol{\sigma}_{\text{kin}} \cdot \mathbf{n}^\alpha) \cdot \mathbf{m}^\alpha \tag{9}$$

The vectors $\mathbf{m}^\alpha$ ($= \mathbf{F}^e \mathbf{m}_0^\alpha$) and $\mathbf{n}^\alpha$ ($= \mathbf{F}^{e-T} \mathbf{n}_0^\alpha$) represent the slip direction and the normal to the slip plane, both of which evolve with deformation. As discussed in [31], the back stress tensor is expressed in terms of scalar kinematic variables Ω^α as

$$\sigma_{\text{kin}} = \sum_\alpha \Omega^\alpha (\mathbf{m}^\alpha \otimes \mathbf{n}^\alpha + \mathbf{n}^\alpha \otimes \mathbf{m}^\alpha) \tag{10}$$

where the components of Ω^α evolve due to the short-range dislocation interactions, in accordance with the equation given in [12] as

$$\dot{\Omega}^\alpha = c\,\dot{\gamma}^\alpha - d\Omega^\alpha |\dot{\gamma}^\alpha| \tag{11}$$

In Eq. (11), c and d are the direct hardening and dynamic recovery coefficients, respectively. Equation (10) takes into account the effect of back stress evolution of one system on all the other systems.

3.2 Implementation in UMAT of the ABAQUS Standard. The time integration and incremental update routine proposed in [25,26] and developed in [16] is incorporated in the user subroutine UMAT of the ABAQUS finite element code. Known deformation variables like the deformation gradient $\mathbf{F}(t)$, the plastic deformation gradient $\mathbf{F}^p(t)$, the backstress τ_{kin}^α, and the slip system deformation resistance $s^\alpha(t)$ at time t, and the deformation gradient $\mathbf{F}(t+\Delta t)$ at $t+\Delta t$ are passed to the material update routine in UMAT. The integration algorithm in the UMAT subroutine updates stresses, plastic strains, and all slip system internal variables to the end of the time step at $t+\Delta t$. An implicit time integration scheme is implemented for integrating the rate dependent crystal plasticity Eqs. (1–11). Various effective implicit schemes have been proposed in literature, e.g., by Anand et al. [25,26], Cuitino, Ortiz et al. [32] using the backward Euler time integration methods. These algorithms are based on the solution of a set of nonlinear algebraic equations in the time interval $t \leq \tau \leq t + \Delta t$ using Newton–Raphson or quasi-Newton solvers. The integration algorithm proposed in [25] and implemented in the user subroutine UMAT of ABAQUS in [33] is adopted in this paper. Known deformation variables like the deformation gradient $\mathbf{F}(t)$, the plastic deformation gradient $\mathbf{F}^p(t)$, the backstress $\boldsymbol{\tau}_{\text{kin}}^\alpha(t)$, and

the slip system deformation resistance $\dot{s}^{\alpha}(t)$ at time t, and the deformation gradient $\mathbf{F}(t+\Delta t)$ at $t+\Delta t$ are passed to the material update routine in UMAT. The integration algorithm in the UMAT subroutine updates stresses, plastic strains and all slip system internal variables to the end of the time step at $t+\Delta t$. The second Piola–Kirchoff stress is first evaluated in this algorithm by solving the following set of nonlinear equations iteratively,

$$\mathbf{S}(t+\Delta t)-\boldsymbol{C}:[\tfrac{1}{2}\{\mathbf{A}(t+\Delta t)-\mathbf{I}\}]$$

$$=-\sum_{\alpha}\ \Delta\gamma(t+\Delta t)(\mathbf{S}(t+\Delta t),s^{\alpha}(t+\Delta t),$$

$$\tau^{\alpha}_{\mathrm{kin}}(t+\Delta t))\boldsymbol{C}:[\tfrac{1}{2}\{\mathbf{A}\mathbf{s}^{\alpha}_{0}+\mathbf{s}^{\alpha T}_{0}\mathbf{A}\}] \tag{12}$$

$$s^{\alpha}_{a}(t+\Delta t)=s^{\alpha}_{a}(t)+\sum_{\beta}\ h^{\alpha\beta}|\Delta\gamma^{\beta}| \tag{13}$$

$$\tau^{\alpha}_{\mathrm{kin}}(t+\Delta t)=\frac{\tau^{\alpha}_{\mathrm{kin}}(t)+c\Delta\gamma^{\alpha}}{1+d|\Delta\gamma^{\alpha}|}, \tag{14}$$

where $\mathbf{A}(t+\Delta t)=\mathbf{F}^{p^{-T}}(t)\mathbf{F}^{T}(t+\Delta t)\mathbf{F}(t+\Delta t)\mathbf{F}^{p^{-1}}(t)$ and $\Delta\gamma^{\alpha}$ is the increment of plastic shear on the slip plane α. The solution is executed using a two-step algorithm, in which the stress $\mathbf{S}(t+\Delta t)$, the slip system resistance $s^{\alpha}(t+\Delta t)$, and the backstress $\tau^{\alpha}_{\mathrm{kin}}(t+\Delta t)$ are each updated iteratively, holding the other unchanged during each iterative cycle. After convergence of the nonlinear equation is achieved, the plastic deformation gradient and the Cauchy stress in each integration point of the element are computed using equations

$$\mathbf{F}^{p}(t+\Delta t)=\left\{1+\sum_{\alpha}\ \Delta\gamma^{\alpha}\mathbf{s}^{\alpha}_{0}\right\}\mathbf{F}^{p}(t) \tag{15}$$

$$\boldsymbol{\sigma}(t+\Delta t)=\frac{1}{\det\mathbf{F}(t+\Delta t)}\mathbf{F}(t+\Delta t)\mathbf{F}^{p^{-1}}(t+\Delta t)$$

$$\times\mathbf{S}(t+\Delta t)\mathbf{F}^{p^{-T}}(t+\Delta t)\mathbf{F}^{T}(t+\Delta t) \tag{16}$$

These are then passed on to the ABAQUS main program for equilibrium calculations. In addition, the Jacobian or tangent stiffness matrix given as $W_{ijkl}=\partial\sigma_{ij}/\partial\varepsilon_{kl}$ is computed in UMAT as well, to be returned to the main program in returned to ABAQUS.

3.3 Orientation Assignment to the Finite Element Mesh. Each grain in the polycrystalline aggregate of HSLA-50 steel is considered to be an element in the finite element model. It is important to assign appropriate crystallographic orientation to the elements prior to FE simulation since deformation response is observed to be highly sensitive to the overall texture. For physically meaningful simulations, crystallographic orientations that are statistically equivalent to those obtained from orientation imaging microscopy (OIM) techniques are assigned to the FE model. The orientation probability assignment method discussed in [34] in conjunction with experimental pole figures, by x-ray diffraction analysis, is used for this purpose. In this method, crystallographic orientations, represented by Euler angles, are first generated from transformed pole figures, in which points in discretized regions of the projected plane are extracted from contour plots of the pole figures in x-ray diffraction analysis. This process generally produces a large number of Euler angles that are considerably in excess of the assignable orientations to the finite element model. Consequently, statistically equivalent orientations with similar probability density distributions $f(g)$ of the crystallographic orientations are assigned to the finite element mesh. The steps in this process are:

i. A Euler angle space in an orthorhombic system [35], is one in which the 3 coordinate axes are represented by 3 Euler angles $(\varphi_1,\Phi,\varphi_2;0\leqslant\varphi_1\leqslant360\ \mathrm{deg},0\leqslant\Phi\leqslant90\ \mathrm{deg},0\leqslant\varphi_2\leqslant90\ \mathrm{deg})$. For bcc metals, a typical positive octant $(0\leqslant\varphi_1\leqslant90\ \mathrm{deg},0\leqslant\Phi\leqslant90\ \mathrm{deg},0\leqslant\varphi_2\leqslant90\ \mathrm{deg})$ corresponding to a reduced Euler angle space is discretized into n (5832 at 5 degintervals) cubic orientation space elements.
ii. From the definition of probability density function, $f(g)\Delta g=\Delta V_g/V$ is the probability of observing an orientation G in the interval $g\leqslant G\leqslant g+\Delta g$, where ΔV_g is the volume of crystals with the orientation between g and $g+\Delta g$ and V is the total volume of all grains. Let $N^{(i)}$ be the number of points in the ith orientation space element ranging from $(\varphi_1,\Phi,\varphi_2)$ to $(\varphi_1+\Delta\varphi_1,\Phi+\Delta\Phi,\varphi_2+\Delta\varphi_2)$ and N the total number of the orientation points in the reduced Euler space. Then, volume fraction of orientation can be written as [17]:
$$V_f^{(i)}=\frac{N^{(i)}}{N}. \tag{17}$$
iii. A orientation probability factor (P_i) for each orientation space element is obtained as
$$P_i=KV_f^{(i)} \tag{18}$$
where K corresponds to a number that is equal to or larger than the number of orientations to be assigned to the finite element mesh. The complete set of statistically equivalent orientations is then given as
$$P=\sum_{i=1}^{n}P_i \tag{19}$$
where P is equal to or larger than the number of grains in the finite element model.
iv. Q $(\leqslant P)$ sets of Euler angles are randomly selected from the orientation population P and are assigned to the integration points of different grains in the computational model. The model with this assigned orientation, represents a statistically equivalent polycrystalline aggregate. Experimentally measured pole figures are compared with and numerically assigned orientations in Figs. 7(a) and (b). All textures are adequately represented in the simulated model.

4 Determination of Material Parameters From Experiments

Systematically calibrated material parameters from experimental results are critical to a meaningful simulation of deformation processes of crystalline materials. Such calibration is a nontrivial effort due to the complexity of the model, as well as the number of parameters involved. Important material parameters include anisotropic elastic constants and crystal plasticity parameters for individual slip systems in each crystal. Together with the description of slip system orientations, geometry and loading conditions, these parameters define inputs to the computational model for deformation analysis, consistent with experiments. The material parameters include (a) the set $X_{\mathrm{el}}=[C_{11},C_{12},C_{44}]$ of three anisotropic elastic stiffness components, (b) the set $X_{\mathrm{flow}}=[\dot{\gamma}_0,\Delta F,P,Q,s_*,s_{a0}]$ of flow related parameters, (c) the set $X_{\mathrm{yield}}=[K,l_p,\dot{\gamma}_{\mathrm{ini}}]$ in the reference strain equations involving dislocation evolution, (d) the set $X_{\mathrm{sl}}=[h_0,s_s,r]$ in the self and latent hardening equations, and (e) the set $X_{\mathrm{kin}}=[c,d]$ in nonlinear kinematic hardening equation. The calibration process entails solving a least-square minimization problem aimed at minimizing the difference between the experimental and simulated values of the stress–strain response. The corresponding problem is stated in terms of an objective or fitness function as:

$$minimize\ \sum_{i}^{M}\left(\sum_{j=1}^{N}(\boldsymbol{\sigma}^{\mathrm{experimental}}-\boldsymbol{\sigma}^{\mathrm{simulated}}(\boldsymbol{\varepsilon}^{\mathrm{experimental}},X))^2\right)_{i,j}$$

$$wrt\ \ X_{\mathrm{el}},X_{\mathrm{flow}},X_{\mathrm{sl}},X_{\mathrm{yield}},X_{\mathrm{kin}} \tag{20}$$

where M is the number of experimental curves and N is the number of the data points for each experiment. In the calibration pro-

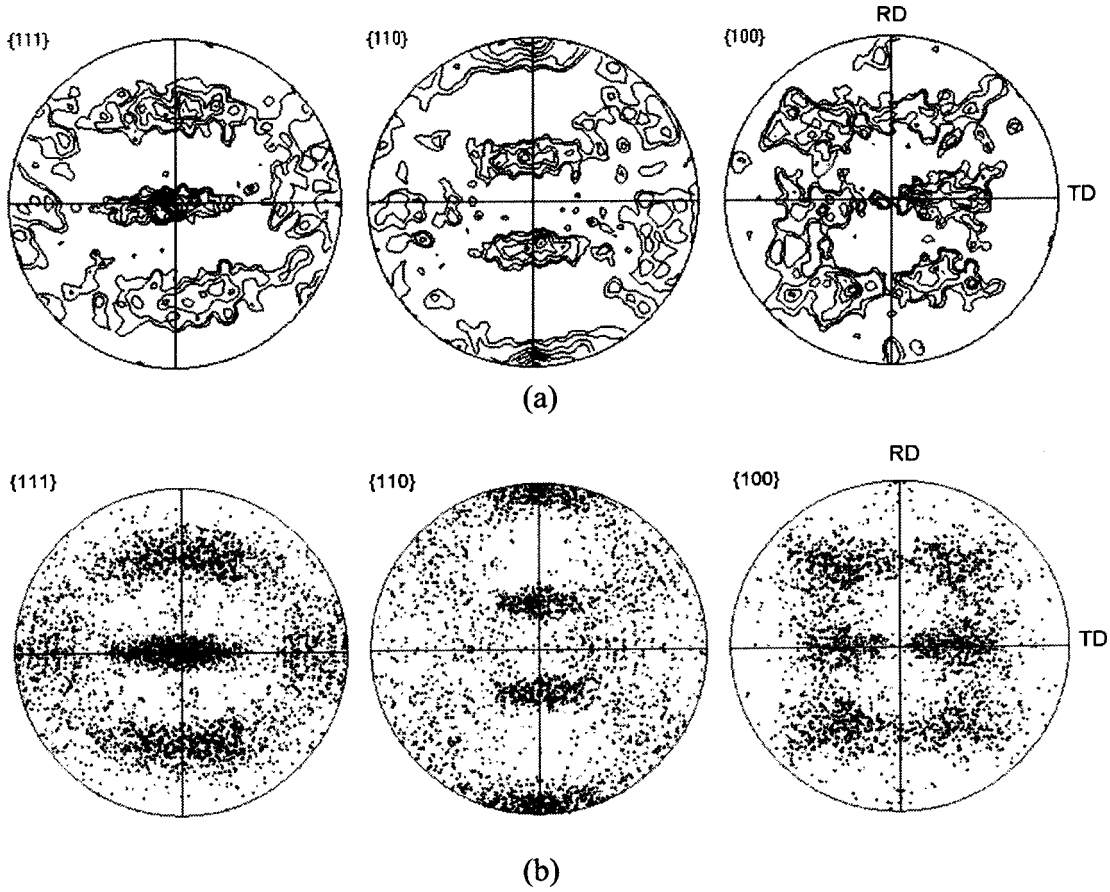

Fig. 7 Pole figures of the polycrystalline HSLA-50 from (*a*) from orientation imaging microscopy and (*b*) simulation using the orientation assignment method

cess, the crystal plasticity parameters for all slip systems are assumed to be the same. The simulation of uniaxial and cyclic tests are performed using ABAQUS standard, with a total of 1728 C3D8 elements in a $12\times12\times12$ array. In the polycrystalline model, each element represents a single grain, for which orientations are assigned from OIM data following steps in Sec. 3.3. For uniaxial tension and strain-controlled cyclic tests, a uniform vertical velocity (along rolling direction) corresponding to the experimental strain rate is applied to the top layer of nodes. The bottom face is constrained to a zero vertical velocity. All the side faces of the cube are kept traction free. For stress-controlled cyclic tests, a uniform vertical tension is prescribed on the top surface. For the uniaxial tension test, M and N in Eq. (20) are 4 (corresponding to four strain rates) and 24 respectively, while the same are 1 and 8 for the cyclic test.

The genetic algorithm (GA) technique of discrete function minimization [36], is implemented for determining the material parameters. A flow chart of the GA based calibration procedure is given in Fig. 8. GA search techniques, which are based on mechanisms of natural selection and natural genetics, start with an initial set of random solutions called populations. Each individual in the population represents a solution to the problem. Each discrete design parameter, corresponding to the sets X, is coded into a binary equivalent string of 0's and 1's and is called a chromosome. The length of the strings or the number of bits that constitute a string depends on the range and resolution with which the design parameter is being represented. A multiparameter binary code is constructed by partitioning each string into a number of compartments equal to the number of parameters being calibrated. After generating chromosomes, the values of the chosen objective function corresponding to the chromosomes are obtained through the analysis module. Each string is next assigned a weight between 0 and 1, which is referred to as its fitness coefficient and is proportional to the magnitude of its objective function. During each generation the chromosomes are evaluated for their fitness and new chromosomes are then generated using 3 genetic operators: (1) Reproduction; (2) Crossover; and (3) Mutation [36]. During each generation the chromosomes are evaluated for their fitness. The two most commonly used genetic operators are crossover and mutation. The procedure is repeated with fitness

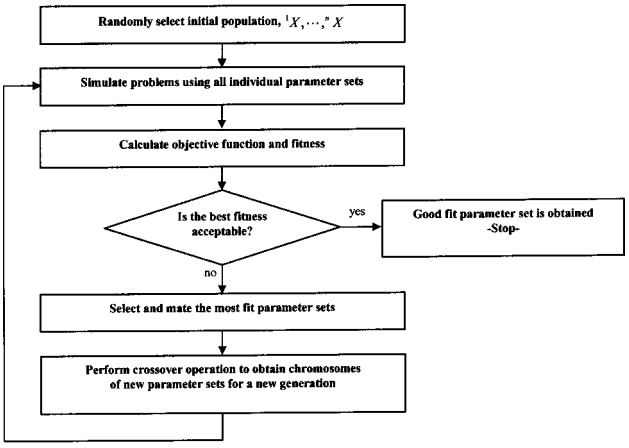

Fig. 8 Flow chart of parameter calibration using genetic algorithms

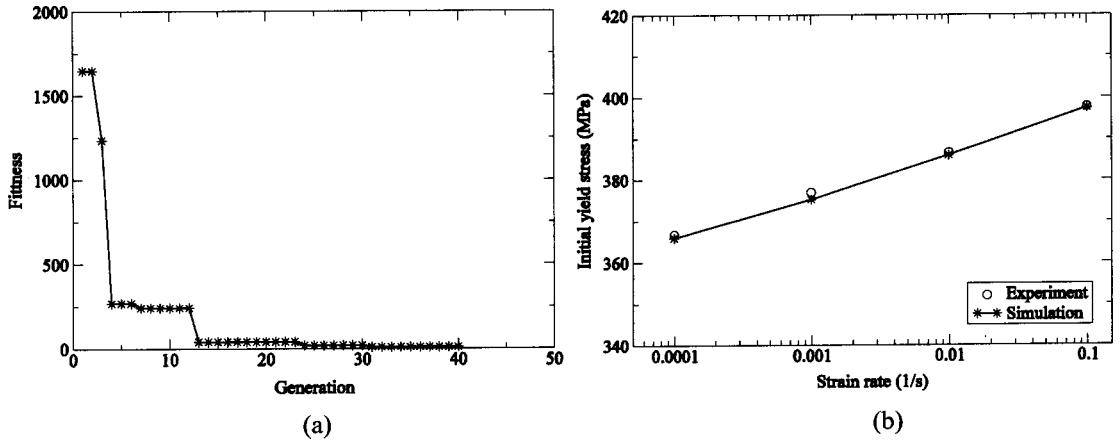

Fig. 9 (*a*) Convergence of the GA in the minimization of initial yield stress as a function of the generation number; (*b*) comparison of experimental and simulated yield strengths as functions of strain rate

coefficients evaluated for each new string. A common practice to stop the iteration is to fix the number of trials in which no further improvement in the value of objective function takes place.

The elastic modules $X_{\text{el}}=[C_{11},C_{12},C_{44}]$, flow parameters $X_{\text{flow}}=[\dot{\gamma}_0,\Delta F,P,Q,s_*,s_{a0}]$ and dislocation multiplication parameters $X_{\text{yield}}=[K,l_p,\dot{\gamma}_{\text{ini}}]$ are determined from the results of the uniaxial tests. For bcc metals, the stiffness component C_{44} is approximately $\approx\mu$, the shear modulus. The flow parameters, some of which lie in the ranges: $1.0\times10^6\leqslant\dot{\gamma}_0\leqslant5.0\times10^7$, $0.05\leqslant\Delta F/\mu b\leqslant2.0$, $0\leqslant P\leqslant1$, and $1\leqslant Q\leqslant2$, are evaluated from the strain-rate sensitivity of the initial yield strength, σ_0. Twenty simulations are done for each generation while the population size is taken to be 5. Figure 9(*a*) shows the GA convergence rate for minimization of a chosen fitness function with the number of generations. Flow and hardening parameters obtained by this calibration process are listed in Table 2. Excellent match is obtained between the experimental and simulated yield strengths at different strain rates using the calibrated parameters, as shown in Fig. 9 (*b*). Furthermore, the simulated stress–strain response for uniaxial tension agrees very well with the experimental response, as shown in Fig. 10(*a*). Finally, the calibrated values of the kinematic hardening parameters $X_{\text{kin}}=[c,d]$ from the stress-controlled cyclic test results are given in Table 2. The corresponding comparison of the stress–strain response under cyclic tension-compression loading is shown in Fig. 10(*b*).

Cyclic plasticity simulations with explicit consideration of slip system evolution through crystal plasticity, are found to yield more accurate results, e.g., with respect to plastic ratcheting, in comparison with results using continuum plasticity models with Armstrong–Frederick kinematic hardening law. These phenomenological models [9,37–39] project averaged material behavior, and are known to overpredict ratcheting. The main reason for such deficiency is that the phenomenological models cannot accurately represent the evolution of slip system variables like back stress, which evolve independently in each slip system depending on the state of evolving variables such as orientation and plastic strain. These individual slip system variables have a strong effect on global variables like overall plastic strain. Averaged continuum models with limited variables are unable to represent this effect. Crystal plasticity modeling has a significant advantage with respect to accurate representation of experimentally observed phenomena such as Bauschinger effect and cyclic hardening/softening, as shown in [10,12–14].

5 Simulation of Deformation in Cyclic Loading of HSLA-50 Steel

The model for polycrystalline plasticity for HSLA-50 steel is now used to simulate the macro and microscale stress and strain responses under cyclic loading conditions. First, the plasticity model for polycrystalline materials is verified by comparing the results of the simulations with experiments for strain-controlled and stress-controlled cyclic loading tests. Subsequently, the effect of grain orientation distributions and overall loading conditions on the evolution of microstructural stresses and strains are investigated. The domain modeled is a unit cube that is discretized into a mesh 1728 eight noded brick elements (C3D8) in ABAQUS-Standard. The mesh is tested for convergence with a more refined mesh. The FE model of the polycrystalline aggregate, consisting of 1728 elements, is assigned a total of 525 crystallographic orientations. The model texture that is assigned using the orientation assignment method discussed in Sec. 3.3, is statistically equivalent to orientation distribution of 11893 OIM data points as shown in Fig. 7. In addition, for the investigations on the texture effects, special orientation distributions are assigned to simulate specific textures with the model. The calibrated elasticity and crystal plasticity material parameters for individual crystals of Sec. 4 are used in these simulations. To emulate experimental conditions, the model applies no symmetry constraints, but only the necessary constraints for suppressing rigid body motion. Velocity and uni-

Table 2 Material parameters of strain aged HSLA-50 steel

Elastic stiffness	Flow parameters	Isotropic hardening parameters	Kinematic hardening parameters	Reference strain rate parameters
$C_{11}=253.1$ (GPa) $C_{12}=132.4$ (GPa) $C_{44}=75.8$ (GPa)	$\dot{\gamma}_0=2.453\times10^7$ (s^{-1}) $\Delta F=2.940\times10^{-18}$ (J) $P=0.7467$ $Q=1.358$ $s_*=120.2$ (MPa) $s_{a0}=85.6$ (MPa)	$h_0=580.1$ (MPa) $s_s=177.1$ (MPa) $r=1.115$	$c=855.0$ (MPa) $d=71.0$	$K=2.01\times10^3$ $l_p=1.90\times10^{-3}$ $a_0=1.05\times10^2$ (1/s) $\varepsilon_L^p=0.014$

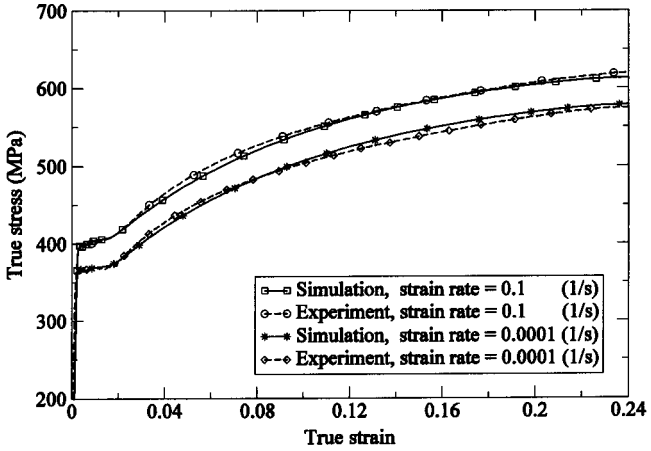

(a)

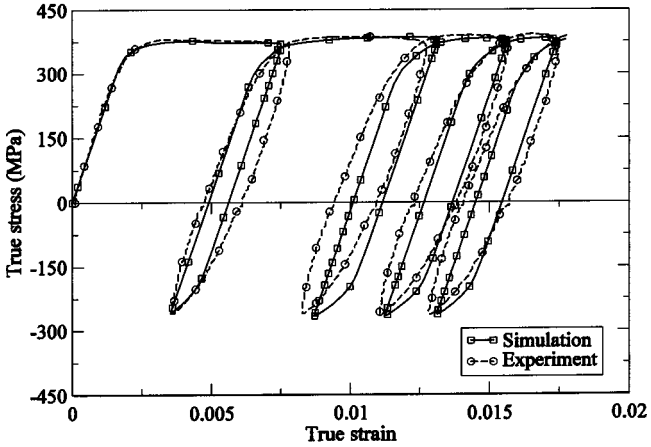

(b)

Fig. 10 Comparison of simulated and experimental stress–strain responses for (*a*) uniaxial tension test and (*b*) stress-controlled cyclic tests

form stress boundary conditions are applied to the top surface corresponding to strain and stress controlled loading, as described in Sec. 4.

5.1 Strain Controlled Cyclic Loading Tests. The two strain-controlled cyclic loading tests discussed in Sec. 2 are simulated in this task. The loading is applied in the form of a velocity corresponding to a strain rate of $\dot{\varepsilon}=\pm 5.8\times 10^{-4}\ \mathrm{s}^{-1}$, in which the strain follows a triangular waveform. The two cases considered correspond to peak strains $\boldsymbol{\varepsilon}_{\max}=0.0045$ and $\boldsymbol{\varepsilon}_{\max}=0.015$ respectively. The average stress–strain response in the direction of the applied velocity is plotted and compared with experiments in Figs. 5(a) and (b). The average stress in the vertical direction (X_2) is calculated as,

$$\overline{\boldsymbol{\sigma}}_{22}=\frac{\sum_{i=1}^{\mathrm{nel}}\sum_{j=1}^{\mathrm{npt}}(\boldsymbol{\sigma}_{22}J)_{ij}}{\sum_{i=1}^{\mathrm{nel}}\sum_{j=1}^{\mathrm{npt}}J_{ij}} \tag{21}$$

where $\boldsymbol{\sigma}_{22}$ is the Cauchy stress and the true plastic strain at each element integration point and $\boldsymbol{J}$ is the determinant of the Jacobian matrix at these integration points. The number of elements is designated as nel, and npt corresponds to the number of integration points per element. For the case with $\boldsymbol{\varepsilon}_{\max}=0.0045$, the simulation shows a small amount of softening due to dislocation multiplication evolution in the first cycle, after which the hysteresis curve stabilizes. For $\boldsymbol{\varepsilon}_{\max}=0.015$, cyclic hardening is observed in the first two cycles due to evolution of isotropic and kinematic hardening, following which the hysteresis curves stabilize. The predicted stress–strain responses agree well with the experimental results.

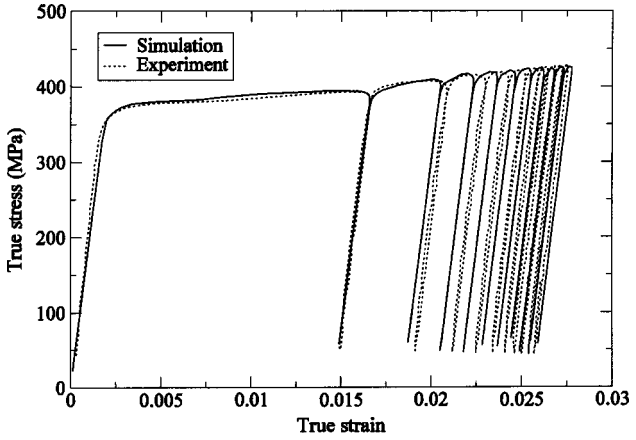

Fig. 11 Stress–strain responses for stress controlled cyclic load testing upto 10 cycles with $\sigma_{\max}$=420.0 (MPa) and R =0.1

5.2 Stress Controlled Cyclic Loading. A stress-controlled tension-tension cyclic load test is simulated with an applied stress in the form of a triangular wave with the following parameters: stress rate $\dot{\sigma}=\pm 226.8$ MPa/s, peak stress amplitude $\sigma_{\max}$ =420.0 MPa, and the R-ratio $R=\sigma_{\min}/\sigma_{\max}=0.1$. However, the P.I.D. controlled MTS servo-hydraulic fatigue machine cannot exactly follow the preset path and the peak stress in the first few cycles because of material transient effects. The corresponding load pattern is also adjusted in the computer simulations to match the experimentally observed variable stress peaks. The simulation is conducted for 10 cycles. There is almost no reverse plastic flow in this case, since the mean stress is positive, As discussed in [9], the cyclic loading path for the rate dependent material properties result in incremental plastic ratcheting with each cycle. This is shown in Fig. 11, which shows excellent agreement between simulated and experimental results.

5.3 Effects of Grain Orientation Distribution on Plastic Deformation. To investigate effects of grain orientation distribution on plastic deformation, simulations are conducted with three different grain orientation distributions, viz. (a) the measured HSLA-50 steel texture of section 3.3, (b) a preferred γ-fiber texture as seen in mild steel [40] and (c) a random orientation distribution. Simulations are conducted with the strain-controlled cyclic loading condition, mentioned in the experimental Sec. 2.2, with triangular strain waveform and peak strain amplitude of 0.0045. The material parameters used are those for HSLA-50 steel, calibrated in Sec. 4. Figures 12(a,b,c) depict the contour plots of the equivalent plastic strain $\overline{\varepsilon}^p$ at the end of 12 cycles. The figures demonstrate the formation of plastic localization bands at 45 deg to the loading axis, especially for the HSLA-50 steel orientation and the microstructure with random orientations. This observation is consistent with experimental results of [41], where small cracks nucleate in the surface grains under cyclic tension-compression. The more random orientations results in higher averaged shear stresses at 45 deg to the loading direction. Localized plastic strain occurs in regions where the orientations are ''soft'' or more favorable to plastic slip, i.e. closer to the

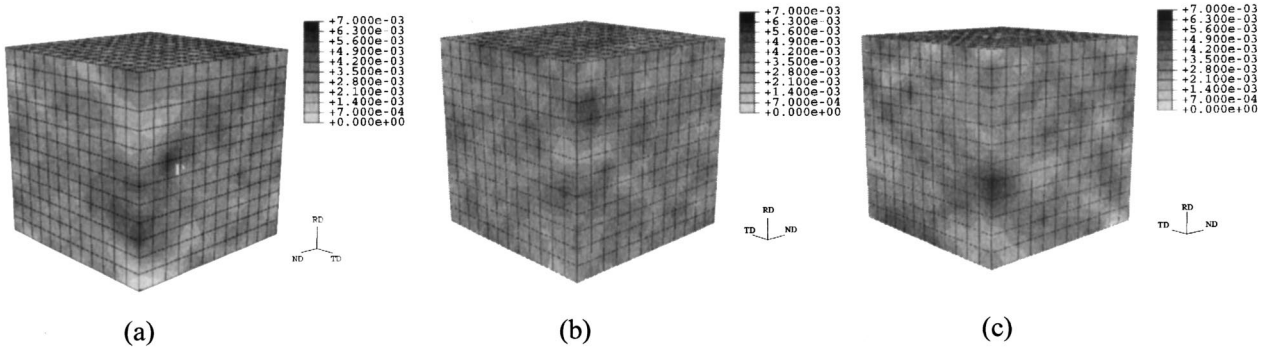

Fig. 12 Distribution of equivalent plastic under strain-controlled cyclic loading at strain amplitude of 0.0045 with (*a*) HSLA-50 steel texture; (*b*) preferred γ-fiber texture; (*c*) random orientation distribution

$\{111\}\langle 110\rangle$ directions. Large departures from the soft orientations are termed as the ''hard'' orientations. Plastic slip is constrained when a ''soft orientation'' is completely surrounded by ''hard orientations'' in which case the localization band cannot grow. Also, the grains on surface, especially at the edges are free to deform independently and regions of high plastic strains are found to originate at these regions. The preferred γ-fiber textured model in Fig. 12(*b*) shows less plastic localization since grains with $\{111\}\langle uvw\rangle$ orientations are all favorable to plastic slip and hence there is significantly less localization. The magnitude and location of the maximum plastic strain vary significantly because of crystallographic texture.

The ratio of the maximum local (micro) equivalent plastic strain $\bar{\varepsilon}^p_{\text{micro}}$ and the volume averaged (macro) equivalent plastic strain $\bar{\varepsilon}^p_{\text{macro}}$, i.e., $R_\varepsilon = \bar{\varepsilon}^p_{\text{micro}}/\bar{\varepsilon}^p_{\text{macro}}$ is plotted as a function of the cycles in Fig. 13(*a*). Under strain-controlled cyclic loading, the average plastic strain is nearly the same for all three orientations. However, the localized plastic strain, which depends on grain orientations, can vary significantly. The local plastic strain is considerably larger for the HSLA-50 steel and the random orientation ($\sim$190%), in comparison with the textured model ($\sim$160%). Figure 13(*a*) shows that the R_ε-ratio is considerably more than 100%, signifying that the local maximum plastic can be much higher than the average strain. The ratio is initially higher and plateaus off at a lower value with increasing averaged strain at higher cycles. In the early stages of loading, the plastic flow concentrates in isolated regions. Subsequently, larger regions yield and extended regions of plastic straining diminish the drop in R_ε leading to a stabilized value. Next, the stress ratio $R_\sigma = \sigma_{\text{micro}}/\sigma_{\text{macro}}$ is plotted in Fig. 13(*b*), where σ_{micro} and σ_{macro} denote the maximum microscopic normal stress and volume averaged stress in loading direction, respectively. All the stress ratios are observed to be less than 1.0. This is due to the fact that stresses are affected by the local orientations as well as plastic flow. The variation for different textures is less for R_σ than that for R_ε.

5.4 Effect of Applied Stress Waveform in Stress-Controlled Cyclic Tests. The effects of the loading waveform on the ratcheting strains may be significant, as mentioned in Chaboche [9]. This example is conducted to investigate the load waveform effects on evolution of plastic strain and ratcheting. For this purpose, two stress-controlled cyclic loadings in the form of a triangular and a sinusoidal loading as shown in Fig. 14(a), are used. The sinusoidal loading has a variable stress rate while the triangular loading has a constant stress rate value. Both the loading cases apply the same amplitude or maximum stress of $\sigma_{\max} = 380.0$ MPa, $R = \sigma_{\min}/\sigma_{\max} = -0.7$, with a time period $T_p = 27.2$ (s). The microstructure and material parameters used are for HSLA-50 steel. Material parameters are the same as those presented in Table 2, with the following exceptions: $s_{a0} = 79.6$ (Mpa), $h_0 = 570.1$ (MPa), $c = 1000.0$ (MPa), $d = 200.0$. A plateau in the stress–strain plot, as discussed in Sec. 3.1 and Eq. (5) is represented by the parameters in Table 2. To examine the influence of this plateau on the ratcheting, a stress–strain plot without the plateau is also considered in the simulations. The lack

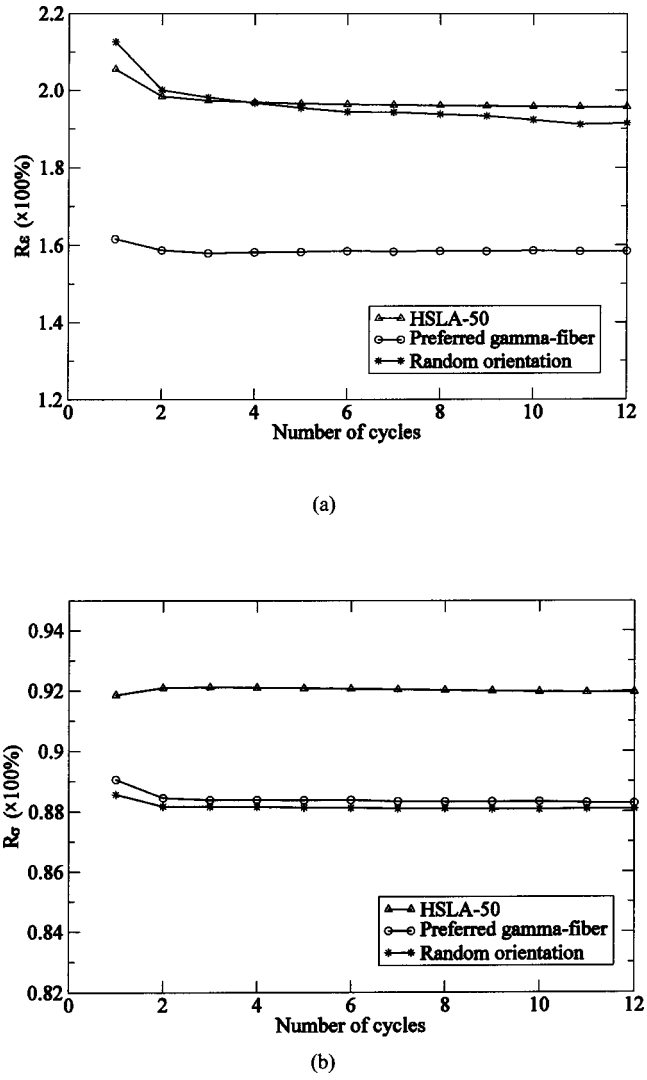

Fig. 13 Ratio of (*a*) local to average plastic strain and (*b*) local to average normal stress in the loading direction, as functions of the cyclic history for three different orientation distributions

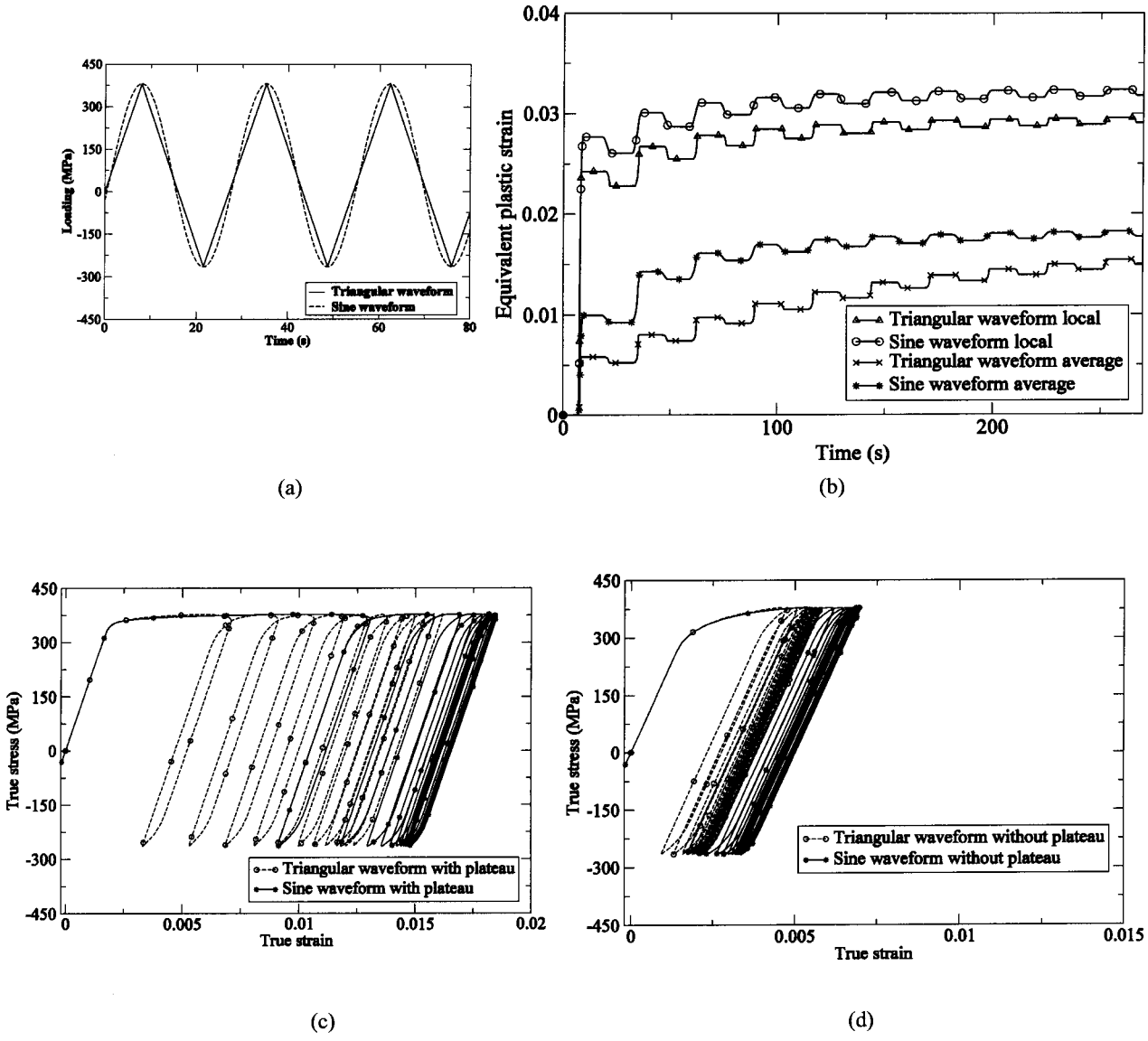

Fig. 14 (*a*) Stress-controlled load histories with different waveforms; (*b*) accumulated microscopic and macroscopic equivalent plastic strains; (*c*) simulated stress–strain response in cyclic loading for material with plateau; and (*d*) simulated stress–strain response in cyclic loading for material without plateau

of plateau in the stress–strain response is obtained through setting the Lüder's strain ε_L^p to zero in Eq. (6) and by choosing $\dot{\gamma}_* = 2.453 \times 10^7$ sec^{-1} in Eq. (5).

Figure 14(b) depicts accumulated microscopic and macroscopic equivalent plastic strains accumulated microscopic and macroscopic equivalent plastic strains during the cyclic loading process. The drops in the plastic strain correspond to reverse plastic straining in the compression phase of loading. The local maximum strain levels are considerably larger than the averaged strain levels over the entire history. The plastic strain produced by the sinusoidal waveform is higher than that by the triangular waveform. This effect is magnified in the plots of Figs. 14(c) and (d), where the simulated stress–strain responses in cyclic loading are shown for materials with and without the plateau. The accumulated equivalent plastic strain, signifying ratcheting, is considerably larger in Figs. 14(c) and (d) for the sinusoidal wave with a variable stress-rate than that for the triangular waveform with a constant stress-rate. Even the small difference in the stresses as shown in Fig. 14(a) is sufficient to cause a considerable difference in the plastic strain due to large material creeps. As seen in Fig. 14(c), the difference is very high for materials like HSLA steels, which have low hardening slopes (plateau) in the early stages of post-yield deformation. Once above yield, large differences in the strains can occur in the early stages of cyclic deformation even for small differences in the applied stress rates. As demonstrated in Fig. 14(d) without the plateau, the incremental differences decrease with increased hardening.

5.5 Effects of Grain Misorientation. A crystal embedded in a polycrystalline aggregate with varying crystal orientations may experience a complex set of tractions and displacement constraints at its interface with its neighbors. Strain localization and stress variation in a polycrystalline aggregate depend on the orientation of the grain with respect to the loading direction as well as misorientations with its neighbors, and mechanical properties of the grain. A finite element model is created with high-angle grain boundaries to reflect the effects of strong heterogeneity in the crystal structure on the local material response. The model is a 120 μm$\times$120 μm$\times$120 μm cube that is discretized into 1728 ABAQUS C3D8 elements in a 12$\times$12$\times$12 array, as shown in Fig.

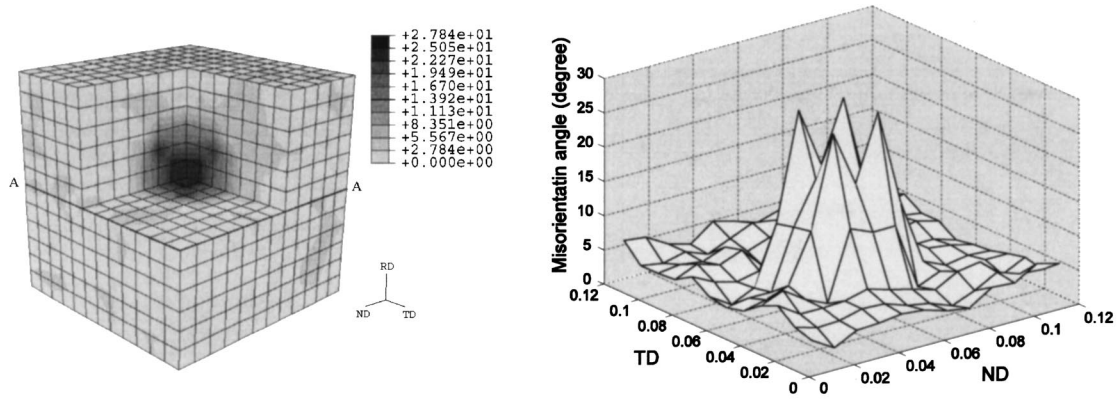

(a) (b)

Fig. 15 Distribution of crystallographic misorientation: (*a*) Quilt-type contours plots; (*b*) 3D plots on section A-A

15(a). It consists of two regions with distinctly different orientation distributions for mismatch in strength characteristics. Region 1 is a 30 μm×30 μm×30 μm cube, with 27 elements all of $\{100\}\langle 110\rangle$ crystallographic orientation that is located at the center. For the outer region 2, selected orientations from the measured ODF data of HSLA-50 steel are assigned to the elements using the orientation assignment method. The general orientation in this region corresponds to $\{111\}\langle 110\rangle$ and grains which have a higher misorientation angle than 5, deg are discarded from the selection. It is common to describe the misorientation in terms of a rotation axis vector **n** and an angle θ. The axis **n** represents a common crystallographic lattice or slip direction for both crystal lattices. The angle θ is the rotation about **n** required to bring the two crystal lattices into coincidence. Using the axis/angle description, the misorientation angle θ between two neighboring grains is described in [42] as

$$\theta = \min\left|\cos^{-1}\left\{\frac{\mathrm{tr}(\mathbf{g}_A\mathbf{g}_B^{-1}\mathbf{O}-\mathbf{1})}{2}\right\}\right| \tag{22}$$

where $\mathbf{g}_A$ and $\mathbf{g}_B$ are the orientation matrixes of grain A and B, respectively, expressed as

$$\mathbf{g}_i = \begin{pmatrix} \cos\varphi_1\cos\varphi_2 - \sin\varphi_1\sin\varphi_2\cos\Phi & \sin\varphi_1\cos\varphi_2 + \cos\varphi_1\sin\varphi_2\cos\Phi & \sin\varphi_2\sin\Phi \\ -\cos\varphi_1\sin\varphi_2 - \sin\varphi_1\cos\varphi_2\cos\Phi & -\sin\varphi_1\sin\varphi_2 + \cos\varphi_1\cos\varphi_2\cos\Phi & \cos\varphi_2\sin\Phi \\ \sin\varphi_1\sin\Phi & -\cos\varphi_1\sin\Phi & \cos\Phi \end{pmatrix}_i, \quad (i=A,B)$$

The angles φ_1, φ_2, *and* Φ are the Euler angles in each grain and **O** is the crystal symmetry operator. Considering that there are 24 identical rotation operations in cubic symmetry, the orientation of each of the two lattices can be described by 24 different symmetrically equivalent rotations. The minimum rotation angle is chosen as the misorientation angle. The average value of misorientation angles for N neighbors of a grain, is given by $\theta_m = (1/N)\,\Sigma_{i=1}^{N}\theta_i$. Figure 15($b$) shows the misorientation distributions near a middle section A-A.

Simulation of a strain-controlled cyclic loading is conducted with strain amplitude of 0.0045. Figures 16(a,b) show the predicted gradient of equivalent plastic strain and stress variation on the section A-A. In region-2, the $\{111\}\langle 110\rangle$ orientation with a large Schmid factor favors plastic flow and hence this region is a ''soft phase.'' In contrast, region-1 with $\{100\}\langle 110\rangle$ orientation is a ''hard phase'' and inhibits large plastic strains. The gradient of equivalent plastic strain $\nabla\bar{\boldsymbol{\varepsilon}}^p = \sqrt{(\partial\bar{\boldsymbol{\varepsilon}}^p/\partial X)^2 + (\partial\bar{\boldsymbol{\varepsilon}}^p/\partial Y)^2 + (\partial\bar{\boldsymbol{\varepsilon}}^p/\partial Z)^2}$ is used as a metric to represent the inhomogeneity in deformations that arise from crystal interactions with high angle misorientation grain boundaries. Large gradients of plastic strain and stress occur along the interfaces between the regions 1 and 2 due to the crystallographic misorientations. When the grains are plastically deformed by slip on specific crystallographic slip systems, the deformations for different orientations are not compatible giving rise to increased stresses and regions of localized straining. Such effects have also been discussed for Ti alloys in [15]. The simulated results in Fig. 16(c) also indicate that the peak stress σ_{22} in the loading direction increases in the first few cycles but finally saturates after 7 cycles. The microstructural effects of grain boundaries and misorientations on ductile failure modes are critical for fatigue cracking. Dislocation densities, high flow stresses at grain boundaries, geometrical softening, the localized accumulation of plastic strain are interrelated physical mechanisms that results in slip-rate impedance and blockage at the grain boundaries, which have been discussed in [15,43,44]. The slip-rate obstruction leads to slip-rate incompatibility at the grain boundary and buildup of normal tensile stresses that can result in the nucleation of transgranular cracks along the primary planes in each grain.

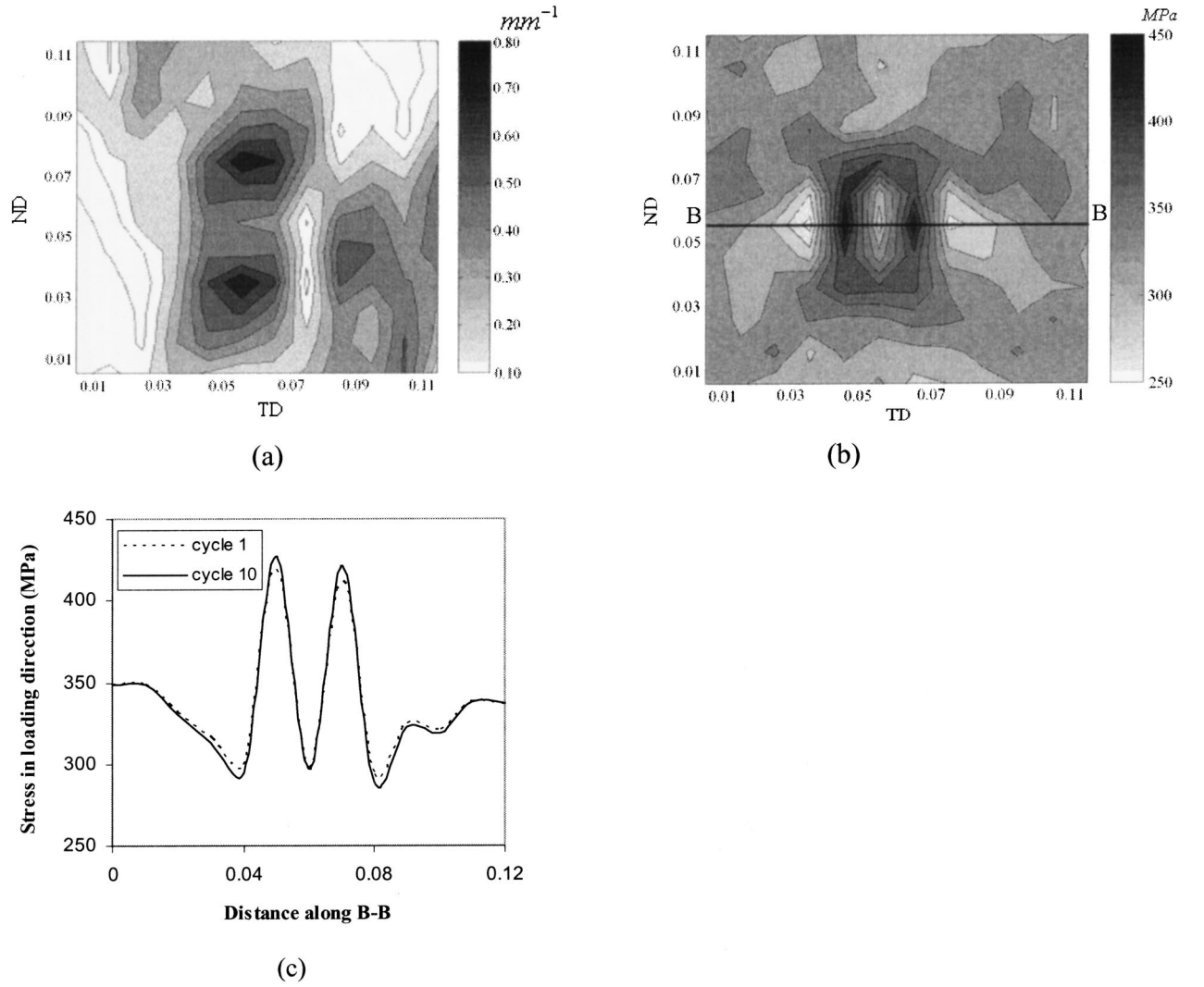

Fig. 16 Distribution of (*a*) gradient of equivalent plastic strain (mm^{-1}); (*b*) stress (MPa) in the direction of loading on the section A-A; and (*c*) evolution of peak stress (σ_{22} in loading direction) along the line B-B

6 Conclusions

The cyclic deformation behavior of metals is of technological importance in the study of fatigue damage. The fatigue process is strongly linked to the microscopic cyclic stress or strain state in a critical region. In an attempt to understand the micromechanical cyclic behavior, the material response of HSLA-50 steel is analyzed in this paper using a rate dependent elastic crystal plasticity model. The paper involves experiments on material characterization and mechanical testing, including OIM, uniaxial tension, and cyclic loading tests for model development and validation. The characteristics of HSLA-50 steel are a predominantly ferrite microstructure with the typical α- and γ-fiber texture, as well as $\{100\}\langle 110\rangle$ orientations. In monotonic loading, a significant yield plateau and strong rate-dependence of yield stress are observed. In strain-controlled cyclic loading, macroscopic cyclic hardening is not found at lower strain amplitudes. In stress-controlled cyclic loading, the build-up of plastic strains and ratcheting is affected by the form of the cyclic load-wave. A rate-dependent elasto-plastic crystalline plasticity constitutive model is developed for simulation of cyclic deformation behavior. This model incorporates self and latent hardening, kinematic hardening, and dislocation multiplication evolution, and is implemented in ABAQUS/UMAT using an implicit time integration scheme. The genetic algorithm technique is utilized to calibrate the material parameters from experimental data.

The computational model is able to reproduce the experimental stress–strain responses in monotonic tension, strain-controlled, and stress-controlled cyclic loading tests with very good agreement. Simulations reveal that the distribution and magnitude of the microscale plastic strain at the level of individual grains is significantly affected by grain orientation distributions. Strain-controlled cyclic test simulations indicate that HSLA-50 steel exhibits higher strain localization than mild steel. The shape of the cyclic load wave is found to affect local plasticity build-up and cause ratcheting. For the same stress amplitude and frequency, the sinusoidal stress waveform produces more accumulated plastic strain than the triangular waveform due to stress rate influence and creep effects. To understand the effect of polycrystalline aggregates on local stress risers, a model with high-angle grain boundaries is created by assigning large orientation mismatch to neighboring grains. This study is important with respect to local crack initiation at critical locations of the microstructure, when subjected to cyclic loading. The simulations show that heterogeneous deformations arise from crystal interactions, especially for high-

angle misorientation grain boundaries, and localizations occur along the interfaces between soft and hard phases. This can serve as a physical motivation for explicit consideration of damage initiation and propagation on the local scale in developing a realistic fatigue model [45,46].

Acknowledgements

The authors are grateful for the financial support of this project provided by the Daimler Chrysler Challenge Fund. In addition the financial support of the OSU-TREP grant is also acknowledged. The authors are particularly thankful to Dr. Yung-Li Lee of the Stress Lab and Durability Development of Daimler Chrysler Corporation for his help and guidance. In addition valuable help of Drs. Marcio Milititsky, Richard Rudy, Ming-Wei Lu, Marlon Forrest, Paul Belanger, Williams Resh, Frank Dosenberger, Sridhar Srikantan, Raymond Segar in the Technical Center of Daimler Chrysler Corporation and Dr. R.E. Tryon of VEXTEC Corporation is gratefully acknowledged. Computer support and resources, provided by The Ohio Supercomputer Center through Grant No. PAS813-2, is also acknowledged.

References

[1] ASM Metals Handbook, 1992, *Properties and Selected Sections of Iron and Steels*, 10th ed., Vol. 1, Metal Parks, Ohio.
[2] Suresh, S., 1991, *Fatigue of Materials*, Cambridge University Press, Cambridge.
[3] Williams, C. R., Lee, Y.-L., and Rilly, J. T., 2003, ''A Practical Method for Statistical Analysis of Strain-Life Fatigue Data,'' Int. J. Fatigue, **25**, pp. 427–436.
[4] Lin, S.-K., Lee, Y.-L., and Lu, M. W., 2001, ''Evaluation of the staircase and the accelerated test methods for fatigue limit distributions,'' Int. J. Fatigue, **23**, pp. 75–83.
[5] Chan, K. S., Pan, Y. M., Davidson, D., and McClung, R. C., 1997, ''Fatigue Crack Growth Mechanisms in HSLA-80 Steels,'' Mater. Sci. Eng., A, **222**, pp. 1–8.
[6] Kannan, K., and Hirth, J. P., 1998, ''Mixed Mode Fracture Toughness and Low Cycle Fatigue Behavior in an HSLA-80 Steel,'' Scr. Mater., **39**, pp. 743–748.
[7] Chung, Y. W., and Lee, W. J., 1994, ''Cyclic Plastic strain Energy as a Damage Criterion and Environmental Effect in Niobium-Bearing High Strength Low Alloy Steel,'' Mater. Sci. Eng., A, **186**, pp. 121–128.
[8] Roven, H. J., and Nes, E., 1991, ''Cyclic Deformation of Ferritic Steel, 1. Stress-Strain Response and Structure Evolution,'' Acta Metall. Mater., **39**, pp. 1719–1733.
[9] Chaboche, J. L., 1991, ''On Some Modifications of Kinematic Hardening to Improve the Description of Ratcheting Effects,'' Int. J. Plast., **7**, pp. 661–678.
[10] Tóth, L. S., Molinari, A., and Zouhal, N., 2000, ''Cyclic plasticity Phenomena as Predicted by Polycrystal Plasticity,'' Mech. Mater., **32**, pp. 99–113.
[11] Mika, D. P., and Dawson, P. R., 1998, ''Effects of Grain Interaction on Deformation in Polycrystals,'' Mater. Sci. Eng., A, **257**, pp. 62–76.
[12] McDowell, D. L., Gall, K., Horstemeyer, M. F., and Fan, J., 2003, ''Polycrystal Orientation Distribution Effects on Microslip in High Cycle Fatigue,'' Int. J. Fatigue, **25**, pp. 27–39.
[13] Morrissey, R. J., McDowell, D. L., and Nicholas, T., 2001, ''Microplasticity in HCF of Ti-6Al-4V,'' Int. J. Fatigue, **23**, pp. 55–64.
[14] Turkmen, H. S., Dawson, P. R., and Miller, M. P., 2002, ''The Evolution of Crystalline Stresses of A Polycrystalline Metal During Cyclic Loading,'' Int. J. Plast., **18**, pp. 941–969.
[15] Hasija, V., Ghosh, S., Mills, M. J., and Joseph, D. S., 2003, ''Modeling Deformation and Creep in Ti-6Al alloys with Experimental Validation,'' Acta Mater., **51**, pp. 4533–4549.
[16] Mika, D. P., and Dawson, P. R., 1998, ''Effects of Grain Interaction on Deformation in Polycrystals,'' Mater. Sci. Eng., A, **257**, pp. 62–76.
[17] Bunge, H. J., 1982, *Texture Analysis in Material Science*, Butterworths, London.
[18] ASME Test Methods of Tension Testing of Metallic Materials, E8M-97, ASTM Book of Standards, Vol. 03.01, 3.1.
[19] Yoshida, F., 2000, ''A Constitutive Model of Cyclic Plasticity,'' Int. J. Plast., **16**, pp. 359–380.
[20] Yan, B., 1998, ''Testing Procedures for Strain Controlled Fatigue Test (Supplement Instructions for A/S P Fatigue Program),'' Daimler Chrysler work report.
[21] Yoshida, F., Uemori, T., and Fujiwara, K., 2002, ''Elastic-Plastic Behavior of Steel Sheets Under In-Plane Cyclic Tension-Compression at Large Strain,'' Int. J. Plast., **18**, pp. 633–659.
[22] Roger, R., and Wagoner, R. H., 2003, ''Development of the Device for Reverse Testing of Sheet Material'' (unpublished).
[23] Balakrishnan, V., 1999, ''Measurement of in-plane Bauschinger effect in metal sheets,'' M.S. thesis, Ohio State University.
[24] Ohno, N., 1982, ''A Constitutive Model of Cyclic Plasticity with a Non-Hardening Strain Range,'' ASME J. Appl. Mech., **49**, pp. 721–727.
[25] Balasubramanian, S., 1998, ''Polycrystalline plasticity: Application to deformation processing of lightweight metals,'' Ph.D. dissertation, Cambridge, MA, MIT.
[26] Kothari, M., and Anand, L., 1998, ''Elasto-Viscoplastic Constitutive Equations for Polycrystalline Metals: Application to Tantalum,'' J. Mech. Phys. Solids, **46**, pp. 51–83.
[27] Peirce, D., Asaro, R. J., and Needleman, A., 1982, ''An analysis of nonuniform and localized deformation in ductile single crystals,'' Acta Metall., **30**, pp. 1087–1119.
[28] Asaro, R. J., and Needleman, A., 1985, ''Texture Development and Strain Hardening in Rate Dependent Polycrystals,'' Acta Mater., **33**, pp. 923–953.
[29] Frost, H. J. and Ashby, M. F., 1982, *Deformation-Mechanism-Map, The Plasticity and Creep of Metals and Ceramics*, Pergamon Press, Oxford.
[30] Kocks, U. F., Argon, A. S., and Ashby, M. F., 1975, ''Thermodynamics and Kinetics of Slip,'' Prog. Mater. Sci., **19**, pp. 141–145.
[31] Harder, J., 1999, ''A Crystallographic Model for the Study of Local Deformation Processes in Polycrystals,'' Int. J. Plast., **15**, pp. 605–624.
[32] Cuitino, A. M., and Ortiz, M., 1993, ''Computational Modeling of Single-crystals,'' Model. Simul. Sc., **1**, pp. 225–263.
[33] ABAQUS reference manuals, 2001, Providence (RI): Hibbitt, Karlsson and Sorenson, Inc.
[34] Xie, C. L., and Nakamachi, E., 2002, ''The Effect of Crystallographic Textures on the Formability of High-strength Steel Sheets,'' J. Mater. Process. Technol., **122**, pp. 104–111.
[35] CHANNEL5 manual, 2001, HKL Technology, pp. 397–340.
[36] Carroll, D. L., 1996, ''Chemical Laser Modeling with Genetic Algorithms,'' AIAA J., **34**, pp. 338–346.
[37] Jiang, R., and Sehitoglu, H., 1994, ''Cyclic Ratcheting of 1070 Steel Under Multiaxial Stress States,'' Int. J. Plast., **10**, pp. 579–608.
[38] Jiang, Y., and Sehitoglu, H., 1994, ''Multiaxial cyclic ratcheting under multiple step loading,'' Int. J. Plast., **10**, pp. 849–870.
[39] Ohno, N., and Wang, J.-D., 1993, ''Kinematic Hardening Rules with Critical State of Dynamic Recovery, Part I: Formulation and Basic Features for Ratcheting Behavior, Part II: Application to Experiments of Ratcheting Behavior,'' Int. J. Plast., **9**, pp. 375–403.
[40] Xie, C. L., and Nakamachi, E., 2003, ''Design of Texture for Improved Formability of High-strength Steel,'' Mater. Sci. Eng., A, **340**, pp. 130–138.
[41] Bennett, V. P., and McDowell, D. L., 2003, ''Polycrystal Orientation Distribution Effects on Microslip in High Cycle Fatigue,'' Int. J. Fatigue, **25**, pp. 27–39.
[42] Kocks, U. F., Tomé, C. N., and Wenk, H. R., 1998, ''Texture and Anisotropy: Preferred Orientations in Polycrystals and Their Effect on Materials Properties,'' Cambridge University Press, Cambridge.
[43] Schmitz, H. A., Dew-Hughes, D., and Bilello, J. C., 1989, ''Nucleation and Propagation of Cracks at GBs in Zinc Bicrystals,'' J. Mater. Res., **4**, pp. 1182–1194.
[44] Zikry, M. A., and Kao, M., 1996, ''Inelastic Microstructural Failure Mechanisms in Crystalline Materials with High Angle Grain Boundaries,'' J. Mech. Phys. Solids, **44**, pp. 1765–1798.
[45] Fujita, H., and Miyazaki, S., 1978, ''Lüders Deformation in Polycrystalline Iron,'' Acta Metall., **26**, pp. 1273–1281.
[46] Imamura, L., Hayakawa, H., and Taoka, T., 1971, ''Contribution of Local Strain Rate at Lüders Band Front to Grain Size Dependence of Lower Yield Stress in Iron,'' Trans. Iron Steel Inst. Jpn., **11**, pp. 191–200.